MNRAS 000, 1–15 (2019) Preprint 20 February 2024 Compiled using MNRAS LATEX style file v3.0

The unbiased frequency of planetary signatures around single and binary white dwarfs using *Spitzer* and *Hubble*

Thomas G. Wilson[1,2]★, Jay Farihi[1], Boris T. Gänsicke[3], and Andrew Swan[1]
[1]*Department of Physics & Astronomy, University College London, London WC1E 6BT, UK*
[2]*Isaac Newton Group, Apartado 321, E-38700 Santa Cruz de La Palma, Spain*
[3]*Department of Physics, University of Warwick, Coventry CV4 7AL, UK*

arXiv:1904.05891v1 [astro-ph.EP] 11 Apr 2019

20 February 2024

ABSTRACT

This paper presents combined *Spitzer* IRAC and *Hubble* COS results for a double-blind survey of 195 single and 22 wide binary white dwarfs for infrared excesses and atmospheric metals. The selection criteria include cooling ages in the range 9 to 300 Myr, and hydrogen-rich atmospheres so that the presence of atmospheric metals can be confidently linked to ongoing accretion from a circumstellar disc. The entire sample has infrared photometry, whereas 168 targets have corresponding ultraviolet spectra. Three stars with infrared excesses due to debris discs are recovered, yielding a nominal frequency of $1.5^{+1.5}_{-0.5}$ per cent, while in stark contrast, the fraction of stars with atmospheric metals is 45 ± 4 per cent. Thus, only one out of 30 polluted white dwarfs exhibits an infrared excess at 3–4 μm in IRAC photometry, which reinforces the fact that atmospheric metal pollution is the most sensitive tracer of white dwarf planetary systems. The corresponding fraction of infrared excesses around white dwarfs with wide binary companions is consistent with zero, using both the infrared survey data and an independent assessment of potential binarity for well-established dusty and polluted stars. In contrast, the frequency of atmospheric pollution among the targets in wide binaries is indistinct from apparently single stars, and moreover the multiplicity of polluted white dwarfs in a complete and volume-limited sample is the same as for field stars. Therefore, it appears that the delivery of planetesimal material onto white dwarfs is ultimately not driven by stellar companions, but by the dynamics of planetary bodies.

Key words: binaries: general – circumstellar matter – infrared: planetary systems – white dwarfs

1 INTRODUCTION

Despite the myriad exoplanetary systems known to exist via transit and radial velocity surveys, knowledge of their chemistry and assembly remains limited. Studies of protoplanetary discs reveal chemical signatures of the solids and gases that precede and are likely incorporated into planetesimals and eventually planets (Bergin et al. 2015; Marty et al. 2017), while exoplanet detection provides the sizes (and sometimes masses) and architectures for a limited set of end results. Direct imaging has demonstrated that wide and massive giant planets are not as frequent as those detected by transit and radial velocity methods, yet these techniques are sensitive only to a fraction of Solar system like architectures (Gillon et al. 2017). The detection of an Earth-like exoplanet around a Sun-like star may be on the horizon, but information on the composition is critical and cannot be provided by conventional means.

From an observational perspective, it is now well established that planetary systems can survive into the post-main sequence. Many white dwarf stars exhibit atmospheric metals that should otherwise sink (Zuckerman et al. 2003; Koester, Gänsicke & Farihi 2014), tens of these display infrared excesses consistent with planetary materials (Reach et al. 2005; Jura, Farihi & Zuckerman 2009), and at least one system has complex transiting events (Vanderburg et al. 2015). These planetary systems orbiting white dwarfs universally exhibit atmospheric metal pollution, where closely-orbiting circumstellar discs – the source of the atmospheric heavy elements – are often detected via dusty and gaseous emission (see Farihi 2016 and references therein). Importantly, white dwarf atmospheres distil the disc material and provide an indirect, but observable elemental composition of the parent body or bodies (see Jura & Young (2014) and references therein). To date, the observed abundances in polluted white dwarfs have been dominated by objects with strikingly Earth-like chemistry (Wilson et al. 2016), but with substantial diversity (Jura et al. 2015; Kawka & Vennes 2016; Hollands, Gänsicke & Koester 2018a), including objects relatively rich in water, but poor in other volatiles (Farihi, Gänsicke & Koester

★ E-mail: tgw@star.ucl.ac.uk

© 2019 The Authors

2013a; Raddi et al. 2015), and a single instance of an ice-rich body (Xu et al. 2017). The nature and frequency of these planetary systems therefore plays a critical and complementary role to the study of the exoplanetary systems via other methods such as transit photometry, precision radial velocities, and direct imaging. No planetary system orbiting a main-sequence star can provide this type of compositional information, and thus polluted white dwarfs are key to understanding the formation and evolution of planetesimals and their associated planets.

Theoretical studies have demonstrated that planet-planetesimal perturbations can create highly eccentric orbits that deliver substantial minor planetary body masses to the innermost orbital regions around white dwarf stars (Veras et al. 2013; Mustill, Veras & Villaver 2014). In some cases, the dynamical interactions are favourable to generating planetesimal orbits with periastra interior to the stellar Roche limit (Debes, Walsh & Stark 2012; Frewen & Hansen 2014), thus leading to tidal fragmentation. In other models, namely those with bodies originating in a Kuiper-like belt, minor body perturbations by a single planet are insufficient to create such star-grazing orbits, and additional (planetary) gravitational encounters are necessary (Bonsor & Wyatt 2012).

In many cases, the delivery of planetary material into the innermost region and eventually onto the white dwarf surface requires full-fledged planets, but their detection has so far been elusive due to insufficient sensitivity (Mullally et al. 2007). The formation of the observed circumstellar discs is an area of ongoing study, where collisions are likely to play a role owing to the fact that the shrinkage of wide and highly eccentric orbits by Poynting-Robertson (PR) drag requires $10^5 - 10^6$ yr or longer for millimetre and centimetre-size particles, respectively (Veras et al. 2015). Once formed, a collision-less disc of solids should evolve via PR drag (Rafikov 2011b; Bochkarev & Rafikov 2011), whether optically thick or optically thin to starlight. If collisions are important or there is significant gas present that is co-spatial with the dust, then competing effects may drive the disc evolution (Rafikov 2011a; Metzger, Rafikov & Bochkarev 2012; Kenyon & Bromley 2017).

A prediction made by dynamical models is that the frequency of white dwarf pollution and circumstellar debris discs should be modestly or strongly time-dependent, based on the nature of the instability that drives material inward (see and compare e.g. Debes et al. 2012; Mustill et al. 2014; Petrovich & Muñoz 2017; Smallwood et al. 2018). Thus, the empirical occurrence rate for atmospheric metals and infrared excesses are necessary to test these models. While the frequency of white dwarfs with photospheric metals has been robustly determined to be at least 20–30 per cent (Zuckerman et al. 2010; Koester et al. 2014), the bulk of published *Spitzer* searches for infrared excesses have targeted stars with known atmospheric metals in order to formalise the link between discs and pollution (Jura, Farihi & Zuckerman 2007; Farihi et al. 2010). To date, the frequency of debris discs that are detected in the infrared has been constrained to be between 1 and 4 per cent (Mullally et al. 2007; Farihi, Jura & Zuckerman 2009; Barber et al. 2012; Rocchetto et al. 2015). However, the bulk of published work has suffered from selection biases, sensitivity issues, or insufficient statistics (or a combination of these). Wide-field surveys such as the Sloan Digital Sky Survey and *WISE* have been utilised to characterise infrared excess frequency using the largest possible number of stars, but can suffer from limited sensitivity and poor sample characterisation (Debes et al. 2011; Girven et al. 2011). Therefore, an unbiased *Spitzer* survey is needed to accurately measure the occurrence of discs that exhibit infrared excesses.

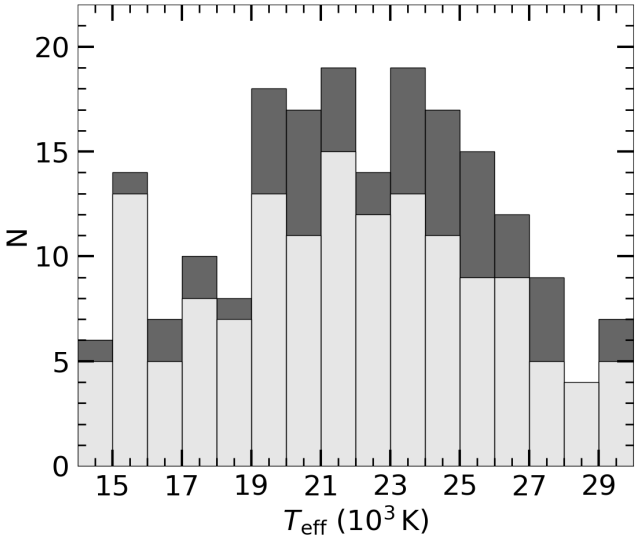


Figure 1. $T_{\rm eff}$ histogram for the single white dwarfs in this study. All stars were observed with *Spitzer* and are shown in dark grey, while the subset observed by *Hubble* are shown in light grey. The same number of targets were observed with both telescopes in one of the bins.

This study analyses *Spitzer* IRAC observations of hydrogen-rich atmosphere white dwarfs that were selected on the basis of cooling age, and thus without any bias toward the potential presence of atmospheric metals. The same stars were part of several *Hubble* COS Snapshots, thereby providing a double-blind study of metal pollution and infrared excess frequency. These observations form the largest available, unbiased *Spitzer* sample to assess infrared excess and atmospheric metal frequencies, and form the only such double-blind study. The *Spitzer* observations are presented in Section 2, with the data analysis reported in Section 3. The results and notes on individual targets are discussed in Section 4, with conclusions given in Section 5. The results of the *Hubble* Snapshots will be discussed in a forthcoming paper.

2 OBSERVATIONS AND DATA

2.1 Sample of single and binary white dwarfs

This paper reports observations that are one part of a dual instrument survey to identify both atmospheric metal and infrared excess frequencies for white dwarfs as a function of effective temperature and hence cooling age. All targets and their associated stellar parameters in the study were taken from catalogues of nearby white dwarfs (Liebert, Bergeron & Holberg 2005; Koester et al. 2009; Gianninas, Bergeron & Ruiz 2011). Sample stars have been selected to have hydrogen-rich atmospheres, owing to their relatively short diffusion timescales (Koester 2009), in order to confidently ascribe any atmospheric metals to ongoing accretion from circumstellar material. Another criterion for each target is $F_\lambda(1300\,\text{Å}) > 5 \times 10^{-14}\,\text{erg cm}^{-2}\,\text{s}^{-1}\,\text{Å}^{-1}$ to achieve a sufficiently high S/N in the far ultraviolet COS spectra. These requirements result in a range of stellar effective temperatures 14 000–31 000 K, and thus probe post-main sequence planetary system dynamics at ages of 9–300 Myr.

The selection criteria above result in 236 sources. An extensive literature and database search indicates that 40 targets are confirmed or candidate binary systems of varying composition and separation. The remaining 196 apparently single white dwarfs form the basis for the bulk of the study. The binary subsample is discussed separately, as the sample statistics are less robust. Table A1 lists all stars for which IRAC photometry was attempted, with binaries noted.

2.2 *Spitzer* observations

Imaging data for the entire sample were obtained with the Infrared Array Camera (IRAC; Fazio et al. 2004) onboard the *Spitzer Space Telescope* (Werner et al. 2004) and are the main focus of this study. The same sample was part of multiple *Hubble* Snapshot surveys using COS, of which 168 targets were observed (cf. 236 observed by *Spitzer*), with the details to be reported in a subsequent publication. New observations for 168 white dwarfs were taken with warm *Spitzer* IRAC in Cycles 8 and 12 for Programs 80149 and 12103, respectively. Targets were observed at both 3.6 and 4.5 μm, where images were taken with 20 frames of 30 s each using the medium-sized, cycling dither pattern, and resulting in a total exposure time of 600 s in each warm IRAC channel. Archival (cryogenic or warm) IRAC observations for an additional 68 sources were retrieved and analysed to complete the sample. As an indication of the survey overlap between instruments, the number of single white dwarfs observed by *Spitzer* and *Hubble* as a function of effective temperature is presented in Fig. 1.

2.3 IRAC photometry

Single, fully processed, and calibrated 0.6 arcsec pixel^{-1} mosaic images were extracted for all targets in the observed bandpasses by the IRAC calibration pipeline S19.2.0. Aperture photometry was conducted using the standard IRAF task APPHOT with aperture radii of 2.4 or 3.6 arcsec, depending on target brightness and additional nearby sources, and 14.4–24.0 arcsec sky annuli. The fluxes were corrected for aperture size using conversion factors listed in the IRAC Data Handbook, but not corrected for colour. For all targets with sufficiently bright neighbouring sources (including binaries), where photometric contamination was possible or likely, PSF-fitting photometry was conducted using APEX. The error in the measured flux was summed in quadrature with the calibration uncertainty that was taken to be 5 per cent (Farihi, Zuckerman & Becklin 2008). The newly measured fluxes and corresponding uncertainties for the entire sample are presented in Table A1. To calculate upper limits, aperture photometry was conducted at the published coordinates using a 2.4 arcsec radius. After aperture correction the determined flux within the aperture was compared to the sky noise per pixel multiplied by the aperture area, with the larger value reported as the upper limit. One target (1339+346) was irreversibly contaminated by a nearby background source, and is not considered further.

It has been shown that intra-pixel variations in the *Spitzer* IRAC detectors can alter the measured flux by a few per cent, especially at 3.6 μm, which could affect the calculated excesses (Mighell, Glaccum & Hoffmann 2008). The pixel-phase response can be modelled by a 2D Gaussian that is offset from the centre of the pixel, with the observed flux variation being determined by the position of the point-spread function (PSF) peak in the pixel. In order to test that the observed fluxes are robust against intra-pixel flux variation, simulations were conducted. Fluxes were calculated by modelling the pixel-phase response at 20 random intra-pixel positions. The average flux variation was determined to be 0.1 per cent. Therefore, with well-dithered observations the flux variation in the analysed mosaicked frames is negligible and errors on the report fluxes will be dominated by measurement and calibration uncertainties.

Spectral energy distributions (SEDs) were constructed for all stars using additional photometric data from various catalogues including: AAVSO Photometric All-Sky Survey (Henden et al. 2016), Deep Near Infrared Survey of the Southern Sky (Epchtein et al. 1999), Panoramic Survey Telescope and Rapid Response System (Chambers et al. 2016), Sloan Digital Sky Survey (Ahn et al. 2012), Two Micron All Sky Survey (Cutri et al. 2003), and UKIRT Infrared Deep Sky Survey (Lawrence et al. 2007). Near-infrared photometric data for several stars were taken from the literature (Farihi 2009; Barber et al. 2012). White dwarf atmospheric models (Koester 2010) were fitted to the available optical through near-infrared fluxes using a least-squares algorithm.

For each star in the sample, model fitting to the available data was conducted starting near the literature value of $T_{\rm eff}$, and varying up to ±2000 K in steps of 500 K. The temperature that resulted in the smallest fitting error was adopted and was typically within 1000 K of the literature value. On average, for a 500 K deviation from the best fit temperature, the model fitting error increased by 7 per cent of the minimal value.

3 DATA ANALYSIS

The following analysis applies only to those single and binary targets where it is possible to recover reliable photometry of the white dwarf. There are 210 such science targets; 195 of these are apparently single, and 15 in spatially-resolved binaries. Those binary systems whose IRAC photometry is dominated or influenced by unresolved or marginally resolved companions are not searched for infrared excesses. However, for many such systems, corresponding COS observations in the far-ultraviolet will effectively probe isolated white dwarfs.

In order to comprehensively establish the frequency of detectable debris discs, two infrared excess determination methods are used: the flux method and the colour method. For each of these methods discussed below, the photospheric model flux is determined by performing synthetic photometry on the atmospheric model over the IRAC bandpasses, with an excess considered significant if it is greater than 3σ. To assess how sensitive the observations are in discovering a debris disc, the minimum detectable excess, η, is calculated for each star. Assuming that excesses are produced by a flat, opaque disc with an inner radius corresponding to $T_{\rm in} = 1400$ K and $r_{\rm out} = {\rm R}_{\odot}$, the η value can be used to determine the inclination, i, at which a debris disc is no longer observable (Bonsor et al. 2017). By calculating the average η values in each warm IRAC channel it is determined that all discs with $i < 89°$ should be detected.

3.1 Method 1: Flux excess

Previous *Spitzer* work searching for warm dust around 180 000 *Kepler* field stars has used the flux excess method (Kennedy & Wyatt 2012). In this method, the observations are compared to the model

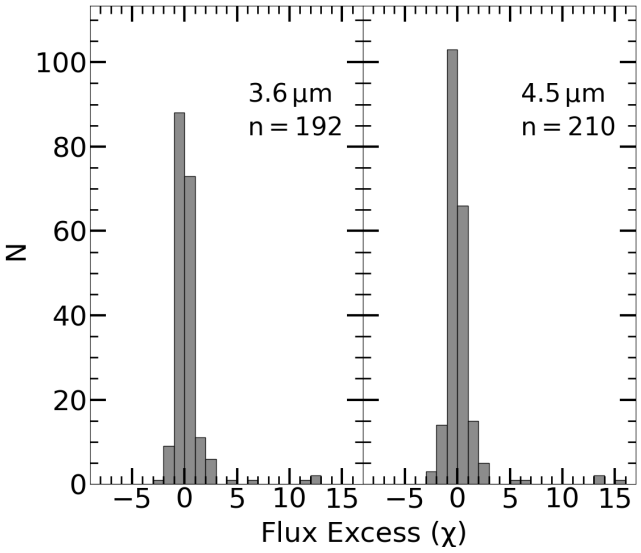


Figure 2. Histograms of flux excess values, χ, as determined by Equation (1) for both warm IRAC channels. It should be noted that not all stars have 3.6 µm data, as some archival targets only have 4.5 and 7.9 µm observations.

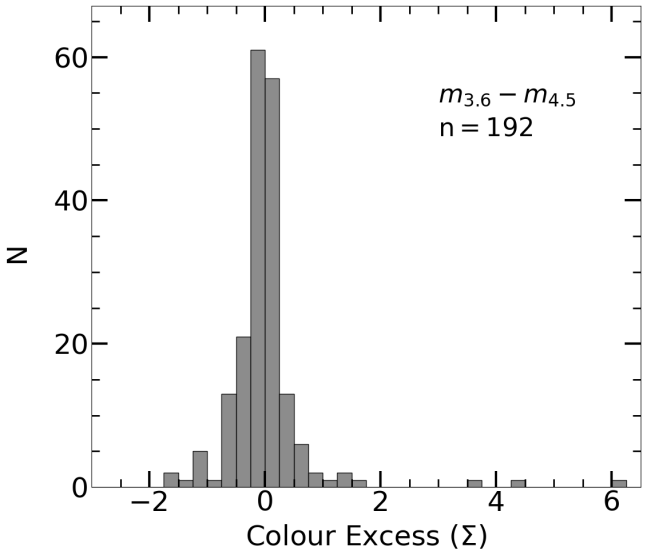


Figure 3. Histogram of $m_{3.6} - m_{4.5}$ colour excess values, Σ, as determined by Equation (2) for stars observed in both warm IRAC channels.

predictions for all IRAC channel measurements using the following statistic.

$$\chi = \frac{F_{\rm obs} - F_{\rm mod}}{\sqrt{\sigma^2_{\rm obs} + \sigma^2_{\rm mod}}} \quad (1)$$

Here $F_{\rm obs}$ and $F_{\rm mod}$ are the observed and model fluxes, respectively, $\sigma_{\rm obs}$ represents the photometric measurement and calibration uncertainties summed in quadrature and are typically 5 per cent of $F_{\rm obs}$. Errors in the model fitting to the short wavelength data are given as $\sigma_{\rm mod}$ and are typically 1 per cent of $F_{\rm mod}$.

Flux excesses, denoted by χ, are calculated using Equation (1), and are plotted as histograms for each warm IRAC channel in Fig. 2. For this sample, the mean and standard deviation in the flux excess statistic are $\langle\chi\rangle_{3.6} = 0.15 \pm 1.07$ and $\langle\chi\rangle_{4.5} = 0.05 \pm 1.15$. These are broadly consistent with Gaussian distributions.

Infrared excess candidates are identified by $\chi > 3\sigma$ in either IRAC bandpass. There are five stars with previously discovered infrared excesses: 0843+516, 1015+161, 1018+410, 1457–086, and 2328+107. All are recovered as significant using this analysis, with χ values in the range 5–15σ, as can be seen in Table 1. Of the remaining sources, two systems exhibit $\chi > 3\sigma$ in both warm IRAC channels and are also reported in Table 1. These two sources – 1132+470 and 2218–271 – are discussed in Section 4.3.

3.2 Method 2: Colour excess

Infrared excess determination via colour can potentially reveal faint debris discs that might be missed using the flux excess method. Examples of excesses calculated on the basis of a single colour, or weighted multiple colours, have been used to detect faint infrared excesses towards main-sequence stars using *WISE* photometry (Patel, Metchev & Heinze 2014; Patel et al. 2017).

In the following method, the observed and model fluxes, and their corresponding errors have been converted into (Vega) magnitudes. The IRAC colour excesses are determined using the following, with all quantities in units of magnitude.

$$\Sigma_{\rm ij} = \frac{m_{\rm i,obs} - m_{\rm j,obs} - m_{\rm ij,mod}}{\sqrt{\sigma^2_{\rm i,obs} + \sigma^2_{\rm j,obs} + \sigma^2_{\rm ij,mod}}} \quad (2)$$

Here *i* and *j* represent the two bandpasses that determine the colour, therefore the numerator in the above equation is the difference between the measured and model colour. The uncertainties in the observed magnitudes are added in quadrature with the uncertainty in the model colour. If sources have infrared photometry in three or more bandpasses, it is possible to construct an excess statistic based on a weighting of the various colours. However, because fewer than 20 per cent of the sample have observations at either 5.7 or 7.9 µm, and given that the longer wavelength arrays are substantially less sensitive (Fazio et al. 2004), these data are not used in the overall assessment. Therefore, this study is restricted primarily to data in the 3.6 and 4.5 µm bandpasses, and thus only a single colour excess statistic is used.

Colour excesses, denoted by Σ, are calculated for all white dwarfs observed with *Spitzer* in both warm IRAC channels using Equation (2), and a histogram of these $m_{3.6} - m_{4.5}$ colour excesses is shown in Fig. 3. The mean and standard deviation are $\langle\Sigma\rangle = 0.02 \pm 0.79$.

Candidates are identified by $\Sigma \geq 3\sigma$, where three stars meet this criterion: 0843+516, 1015+161, and 1018+410. It is immediately apparent that this technique missed four stars that are flagged by the flux excess method (1132+470, 1457–086, 2218–271, and 2328+107; see Section 4.3). The Σ values for these stars are reported in Table 1. This method may be powerful when multiple infrared bandpasses are available, as this adds information that is not present with only IRAC 3.6 and 4.5 µm photometry. As it stands, for the subsample with data in both channels, the flux excess method is more sensitive, especially to SEDs that deviate modestly from a Rayleigh-Jeans slope. Interestingly, only white dwarfs with $\chi > 10\sigma$ are seen to have a corresponding $\Sigma > 3\sigma$ as shown in Fig. 4, but this can be partly accounted for by the additional un-

Table 1. Infrared excess statistics for stars with values above 3σ using at least one method. Columns are named after the wavelength in microns at which the excesses are determined.

WD	..... χ ..... (3.6)	(4.5)	..... Σ ..... ($m_{3.6} - m_{4.5}$)
0843+516	12.9	15.4	6.1
1015+161	11.8	13.7	3.8
1018+410	12.3	13.2	4.4
1132+470	7.6	7.3	0.0
1457–086	6.0	6.0	0.2
2218–271	6.2	7.9	1.9
2328+107	4.9	5.5	0.6

certainty of utilising two measurements for colour excesses (Patel et al. 2014). Although the stars flagged by the colour excess method are fewer, the results in Section 4 demonstrate they are a higher fidelity sample of bona fide discs.

3.3 Atmospheric metals

Hubble COS data were obtained for a subsample of stars that also have *Spitzer* IRAC measurements. The analysis of these ultraviolet spectra requires detailed atmospheric modelling, including the effects of radiative levitation, and is beyond the scope of this paper. A subset of the *Hubble* spectra has been published in Koester et al. (2014), and the full dataset is the subject of ongoing work. This study focuses on the frequency of discs detectable in the infrared with *Spitzer*, but a fundamental issue is sensitivity to circumstellar material, as it is established that many metal-enriched stars lack infrared excesses (Rocchetto et al. 2015; Farihi 2016). For this reason, a visual inspection of the *Hubble* spectra is conducted, with the absence or presence of Si II noted. Among 168 observed stars, 78 exhibit photospheric silicon.

4 RESULTS

Below, the results are presented separately for those apparently single white dwarfs versus those confirmed or suspected to be in binary systems.

4.1 Single white dwarfs

Using the methods outlined above, out of the 195 nominally single white dwarfs with good IRAC photometry, seven systems display a significant infrared excess. However, as discussed in more detail below, not all of the excesses are thought to be due to planetary debris discs. There are three potential causes of infrared excesses: circumstellar debris discs, binary companions, or background contamination. This subsection focuses on three excesses thought to be due to debris discs, while Section 4.3 discusses three systems whose excesses are possibly consistent with binarity and one with contamination.

These stars and excess values are reported in Table 1. Interestingly, it should be noted that the three systems with an excess due to a planetary debris disc have significant excesses using both methods, whereas the objects with an excess that can be explained by other causes only have a significant excess using the flux method. This apparent link between bona fide discs and significant excesses

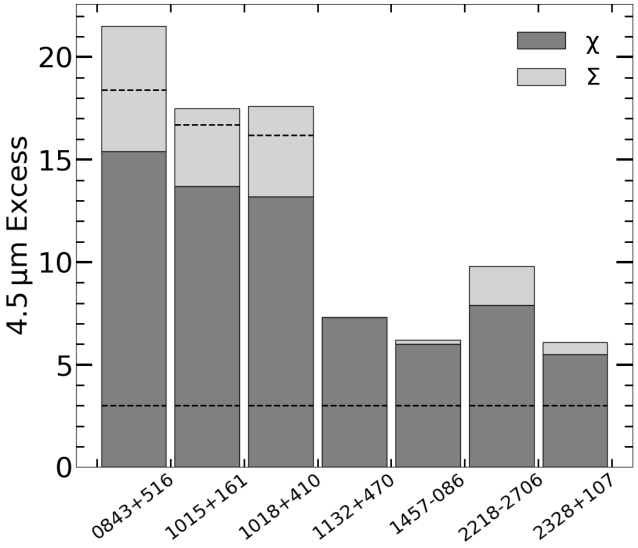


Figure 4. Photometric excesses at 4.5 μm as determined by both methods. The black dashed lines represent 3σ for each method. Only three stars with bona fide debris discs have a significant infrared excess using both methods.

in both methods can be seen clearly in Fig. 4. Furthermore, by calculating the excesses of known dusty white dwarfs using both methods it can be seen that 92 per cent have a significant excess using both the flux and colour methods.

The following analysis is restricted to the apparently single white dwarfs in the sample for which there is *Spitzer* photometry at 4.5 μm, and the subset of these that have *Hubble* data (see Table 2), in order to determine the frequency of infrared excesses and atmospheric metals that can be attributed to a planetary system. The nominal frequency of infrared excesses at single stars due to debris discs within the sample is 3/195 ($1.5^{+1.5}_{-0.5}$ per cent) whereas it is 65/143 (45 ± 4 per cent) for atmospheric metals, with the uncertainties calculated using the binomial probability distribution with a 1σ confidence level. As both observations are indicators of circumstellar debris, it is interesting to see that *the overwhelming majority of stars with debris discs do not exhibit an infrared excess.*

These results broadly agree with previous infrared studies, but at the lower end of estimates made over the years since the launch of *Spitzer*. Some of the earliest estimates determined infrared excess frequencies due to planetary debris discs of 1–2 per cent (Mullally et al. 2007; Farihi et al. 2009; Debes et al. 2011), and this study now robustly establishes this fact. Interestingly, there have been estimates as high as 4 per cent, even including a substantial subset of the stars studied here (Barber et al. 2012; Rocchetto et al. 2015), and thus the benefit of the largest sample available, homogeneous selection and data, plus careful vetting are evident. This result holds for the *Hubble* subsample where the infrared excess frequency at single stars due to planetary debris is $1.4^{+1.8}_{-0.4}$ per cent.

The wide temperature range of this unbiased sample is unprecedented, and permits an assessment of the frequency of infrared excesses at single stars due to debris discs as a function of post-main sequence planetary system age. Fig. 5 plots the fraction of single white dwarfs with infrared excesses due to debris discs as a function of cooling age. To the level of the available data, the infrared excess frequencies around single stars due to debris discs appear to be flat across the entire cooling age range probed in this study, and of the order of a few per cent.

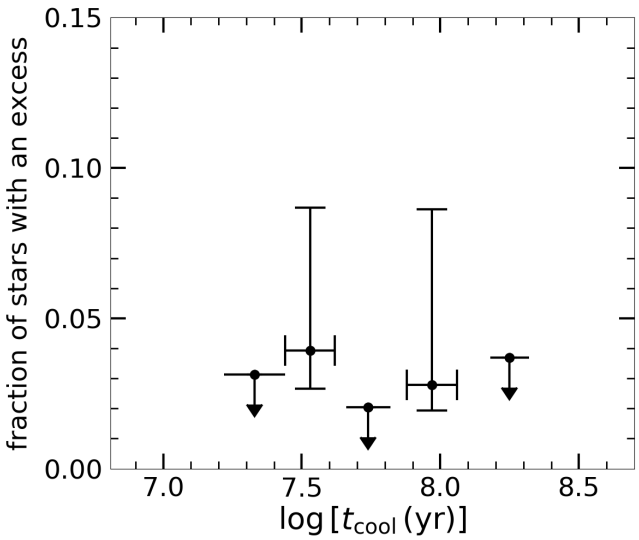


Figure 5. The fraction of single stars in the sample with an infrared excess due to a debris disc, with 1σ binomial probability errors and upper limits, for several cooling age bins.

The combined use of *Spitzer* infrared imaging photometry and *Hubble* far-ultraviolet spectroscopy is unprecedented for such a large sample of white dwarfs. Also, these two telescopes provide the most sensitive observations of atmospheric metals and infrared excesses, and therefore comparison with other studies will be biased. For the temperatures studied here, the results should be highly robust. However for cooler stars that do not emit sufficiently in the far-ultraviolet, the frequency of infrared excesses and atmospheric metals have a mixture of empirical constraints. In the study of Zuckerman et al. (2003), for stars cooler and older than the present study with $T_{\rm eff} < 14\,000$ K, there is only one star out of 70 that did not have a previously known infrared excess ($1.4^{+3.1}_{-0.5}$ per cent), but 18 of these were newly found to have metal absorption features (26^{+6}_{-4} per cent). Infrared excess searches around polluted white dwarfs with $T_{\rm eff} < 10\,000$ K have resulted in only one or two possibly bona fide detections (Farihi et al. 2008; Xu & Jura 2012; Bergfors et al. 2014; Debes et al. 2019).

Despite having observed nearly 200 stars, it can be seen in Fig. 5 that there are cooling age bins without infrared disc detections. This is particularly interesting for two reasons. First, the *Hubble* observations, as well as many ground-based studies, have shown that the fraction of polluted white dwarfs is at least an order of magnitude greater than the fraction of stars with an infrared excess due to a circumstellar debris disc. Second, early indications appear to favour a flat distribution of atmospheric metals as a function of cooling age (Gänsicke et al. 2012), although the full effects of radiative levitation need to be reckoned. The dearth of infrared excesses compared to atmospheric metals supports the idea that circumstellar discs orbiting white dwarfs are typically relatively narrow, or in other ways tenuous (Farihi et al. 2010; Rocchetto et al. 2015; Bonsor et al. 2017). This idea may be supported by the narrow, eccentric ring of debris seen transiting WD 1145+017 (Redfield et al. 2017; Cauley et al. 2018).

4.2 Binary white dwarfs

Recent theoretical work has suggested several, long-term dynamical processes involving a binary companion that may significantly contribute to white dwarf atmospheric pollution (Bonsor & Veras 2015; Hamers & Portegies Zwart 2016; Petrovich & Muñoz 2017; Stephan et al. 2017; Smallwood et al. 2018). While it is clear that a stellar wind from a companion in a short-period orbit may deliver heavy elements onto a white dwarf (Debes 2006; Tappert et al. 2011), for systems with sufficiently wide orbits any detectable pollution requires a non-stellar reservoir of material (Farihi et al. 2013b; Veras et al. 2018). Auspiciously, white dwarf stars are highly transparent to companion detection via their Earth-sized radii and blue-peaked stellar continua; only the coldest and lowest mass substellar companions remain out of reach of conventional, ground-based detection (Farihi, Becklin & Zuckerman 2005).

In the following subsections, the 40 science targets in known or suspected binaries are evaluated. A search using both *Gaia* DR2 and via the literature recovers 22 known spatially-resolved and common proper-motion companions (e.g. El-Badry & Rix 2018), and no new candidates, whereas 18 other white dwarfs are confirmed or suspected to be in short-period binaries. Spatially-unresolved or marginally-resolved IRAC targets (25 sources, including all suspected close binaries) did not produce reliable photometry of the white dwarf itself and are removed from the infrared statistics, leaving 15 white dwarfs in wide binaries that can be searched for photometric excess due to circumstellar dust. However, in the far-ultraviolet with COS, only the white dwarf contributes flux, and thus all 22 sources that are spatially resolved in *Gaia* DR2 are retained in the study of pollution frequencies. Below, infrared excesses and atmospheric pollution are discussed sequentially, using the double-blind study together with independent samples of stars to assess the potential relationships of these phenomena with white dwarfs in wide binaries. The resulting statistics are listed in Table 2.

The following evaluates available data on infrared excesses and wide binarity among white dwarfs. Within the infrared study presented here, all targets confirmed or suspected to be in wide binaries were analysed in an identical manner to the single stars. For the 15 white dwarfs in wide binaries (14 systems; both white dwarfs in 2220+217 are in the sample) that are resolved in their respective IRAC images, there are none with significant flux or colour excess. This yields a binomial probability upper limit of 8 per cent for infrared excesses due to debris discs around white dwarfs with a wide binary companion. While this result is not as robust as the fre-

Table 2. Subsample statistics for infrared excess and pollution.

Description	n	m	m/n
Singles in this study:			
Infrared excess $\chi > 3$	195	3	0.015
Metals detected by *HST*	143	65	0.455
Binaries in this study:			
Infrared excess $\chi > 3$	15	0	0
Metals detected by *HST*	12	8	0.667
Published data:			
Wide companions to dusty stars	40	0	0
20 pc sample:			
Metals among binary stars	29	5	0.172
Binaries among polluted stars	23	5	0.217
Binaries in the 20 pc stars	139	29	0.209

Notes. The second and third columns are the sample size and those targets that meet the condition, respectively, while the last column is the fraction that satisfy the criterion.

quency for single white dwarfs, below a much stronger statement can be made based via confirmed dusty stars with infrared excesses.

Starting from 40 polluted white dwarfs with well-established infrared excesses (e.g. Table 3 of Rocchetto et al. 2015), *Gaia* DR2 enables the straightforward detection of wide companions such as those favoured by dynamical models to enable pollution mechanisms. This search of known dusty white dwarfs returns no bona fide, co-moving companion candidates.[1] [Interestingly and although speculative, a quasi-co-moving companion to SDSS J073842.57+183509.6 ($\varpi = 5.8 \pm 0.2$ mas, $\mu = (12.8 \pm 0.3, -24.1 \pm 0.2)$ mas yr^{-1}) was identified at a projected separation of 0.54 pc and of approximate mid-M spectral type ($\varpi = 5.9 \pm 0.1$ mas, $\mu = (9.8 \pm 0.1, -23.7 \pm 0.1)$ mas yr^{-1}). No claim is made here that the pair are related or evaporating, but it is noteworthy that even in the case this system was previously bound, the white dwarf likely evolved essentially as a singleton rather than a binary.] Therefore, it does not appear that binarity has any physical prominence in the generation of dusty debris discs orbiting white dwarfs.

The possible connection between atmospheric pollution and the presence of a wide companion is explored in the following paragraphs. In the double-blind study sample of white dwarfs, eight out of 12 wide binary targets exhibit atmospheric metals in either *Hubble* Snapshot or published ultraviolet observations, resulting in a frequency of 67^{+10}_{-15} per cent. While the nominal value may seem high, it is within 2σ of the pollution frequency robustly measured for single stars (Zuckerman et al. 2010; Koester et al. 2014). Again due to small number statistics of the present study, below a more robust assessment can be made based on larger and well-studied samples.

An independent assessment of metal pollution and wide binarity can be made using the 20 pc white dwarf sample that is thought to be complete based in *Gaia* DR2 (Hollands et al. 2018b). First, the probability of atmospheric pollution given binarity is evaluated. There are 29 binary systems containing at least one white dwarf, where five systems have a component with atmospheric metal pollution. Thus, in the 20 pc sample there is a 17^{+9}_{-4} per cent probability of pollution among white dwarfs in wide binaries (this is actually a lower limit as not all stars have ultraviolet observations). It is noteworthy that this frequency is nearly identical to that derived solely on the basis of high-powered optical and ultraviolet spectroscopic surveys (Zuckerman 2014).

Second, the probability of binarity given atmospheric pollution is calculated. The 20 pc sample (Hollands et al. 2018b) contains 29 multiples among 139 systems, and thus has a multiplicity fraction of 21^{+4}_{-3} per cent. Within the same sample, there are 23 polluted white dwarfs where five are in binaries (22^{+11}_{-6} per cent). Both these multiplicity fractions are consistent with each other, and with that of deeper field star surveys for a larger number of sources (Farihi et al. 2005). Therefore, it appears that polluted white dwarfs are members of binary systems at the same frequency as field white dwarfs, and that binarity does not play a fundamental role in their nature as metal-enriched stars.

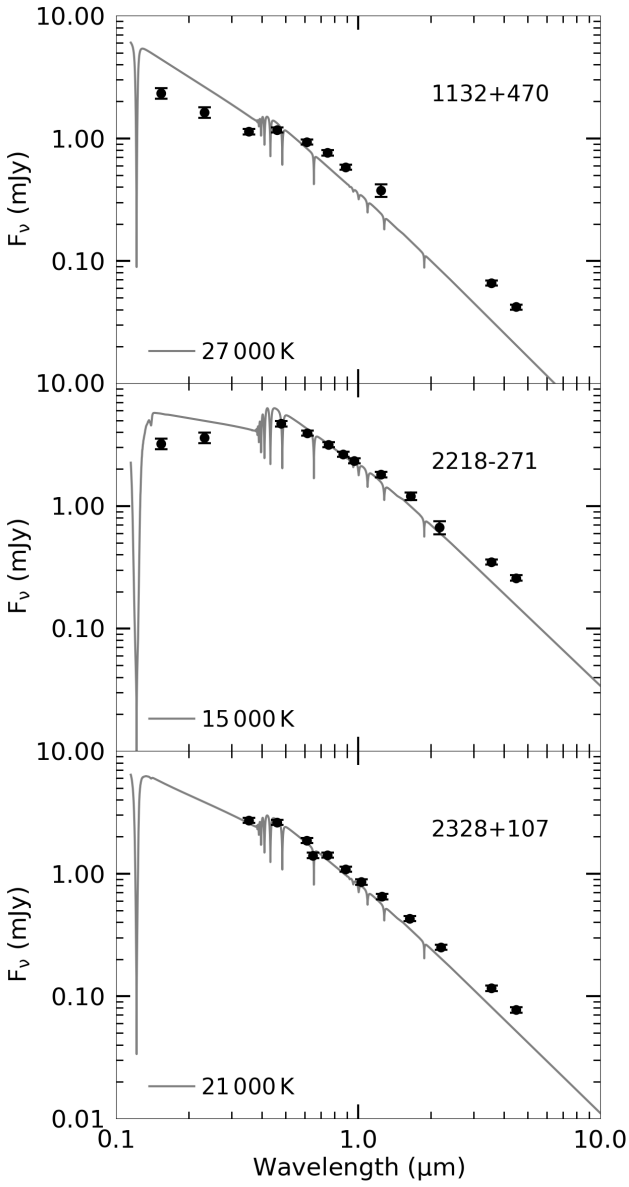


Figure 6. SEDs of three stars with significant infrared flux excesses. Data points with error bars are the *Spitzer* photometry together with shorter wavelength fluxes taken from the literature, and the grey lines represent the white dwarf atmospheric models. All models have $\log g = 8$ with $T_{\rm eff}$ given in the plots. *GALEX* photometry is shown, but excluded from the fitting process, as observations can suffer from interstellar extinction.

4.3 Notes on Individual Objects

Five white dwarfs in the sample have previously identified infrared excesses (Jura et al. 2007; Farihi et al. 2009; Xu & Jura 2012; Rocchetto et al. 2015). Four stars (0843+516, 1015+161, 1018+410, and 1457–086) show metal features in COS ultraviolet spectra (Gänsicke et al. 2012; Koester et al. 2014). One disc candidate exhibits a particularly modest flux excess and is discussed

[1] The only binary among dusty and polluted white dwarfs is the short-period system SDSS J155720.77+091624.6 (Farihi, Parsons & Gänsicke 2017), where the disc must be *circumbinary*, and hence the companion is not suspected of dynamical delivery of the observed material.

below. Finally, 2328+107 displays a subtle ($\chi > 4\sigma$) flux excess in both warm IRAC channels, however it *does not exhibit atmospheric metals in the ultraviolet*, as obtained with COS. This star is also discussed below.

1132+470. This star is one of two white dwarfs in the USNO parallax programme that exhibited unambiguous residual astrometric motion over decades of observation. Both this object and 1639+153 (= LHS 3236) have clear astrometric periods of several years, and with companions identified as white dwarfs via adaptive optics (Subasavage et al. 2009; Harris et al. 2013). This is consistent with the finding that the photometric and spectroscopic effective temperatures are highly discrepant (Bédard, Bergeron & Fontaine 2017). The SED shown in Fig. 6 demonstrates the spectroscopic $T_{\rm eff}$ is not a good fit to the available multi-wavelength photometry.

2218–271. This target exhibits a significant infrared flux excess (Fig. 6), but no photospheric metals are detected in ultraviolet spectroscopy with COS. There is no published study that indicates binarity for this star, but there appears to be photometric excess in both the near-infrared and longer wavelengths. This fact makes it unlikely that the *Spitzer* observations suffered from background contamination, but this possibility was tested by measuring PSF roundness with the IRAF task DAOFIND. The IRAC 4.5 μm image of 2218–271 has a roundness value of 0.06, where the average of 20 field stars in the same image is 0.08 ± 0.10 (a value of 0 is perfectly round). Moreover, the *Spitzer* sample of single stars has an average roundness of 0.09 ± 0.05, and thus the source of the excess is likely due to an unresolved stellar or substellar companion.

During the ESO SN Ia Progenitor Survey (SPY; Napiwotzki et al. 2003), this system was observed twice with UVES, separated by 16 d, in order to probe for short-period radial velocity variations. While the UVES heliocentric-corrected velocities of the H α lines agree within the errors, there is a promising 5.3 h period signal (S. G. Parsons, private communication) in photometric data from the Catalina Real-time Transient Survey (CRTS; Drake et al. 2009). Further observations are needed to confirm this candidate photometric period, and to further constrain the potential binary properties of this system. The *Gaia* DR2 astrometric data for 2218–271 are consistent with a single source.

2328+107. The infrared excess toward this star has been previously reported (Rocchetto et al. 2015) and can be seen in Fig. 6. While the initial discovery was fitted with a relatively narrow disc model, there are no atmospheric metals present in the ultraviolet COS spectrum. Similar to 2218–271, this source has no previously published indications of binarity, and exhibits photometric excess not only at warm IRAC wavelengths, but also in the near-infrared compared to the adopted atmospheric model. An assessment of IRAC 4.5 μm PSF roundness is performed for 2328+107, where a value of 0.02 was determined, which agrees well with the value determined for the single white dwarfs observed in the study as well as 20 field stars (0.09 ± 0.04) within the same image. Thus while the observed infrared excess is possibly, but unlikely, due to contamination, it may be more likely that 2328+107 has a stellar or substellar companion.

To assess the possibility of a short-period companion, the radial velocities of H α are compared between two SPY UVES spectra taken 3 d apart. No significant variations are seen in heliocentric-corrected data, and *Gaia* DR2 astrometry is consistent with that of a single source. Further observations are required to confirm or rule out the possible phase space for companions to this white dwarf, as photometric data from CRTS do not reveal any obvious variability.

1457–086. This is one of the most highly metal-polluted white dwarfs known (Koester et al. 2005). However, archival 2010 and 2013 adaptive optics images from the VLT reveal the presence of a background source within 0.4 arcsec of the star (Dennihy et al. 2017). This calls into question the nature of the observed infrared excess, and it is unclear to what extend the faint background source – detected so far only in the J-band – contributes to the SED at IRAC wavelengths.

As above, the PSF roundness at 4.5 μm is examined in the 2006 IRAC image for evidence of additional sources. The target has a roundness of 0.07 that is comparable to that for 20 field stars in the same image (0.05 ± 0.04), and for the single star sample. However, there is a second IRAC epoch of this degenerate taken in 2017, and while the 4.5 μm flux is unchanged from that measured in 2006, the PSF roundness of the target is 0.54 in 2017. The average roundness for 20 field stars in the same 2017 image is 0.06 ± 0.05, and hence the elongated PSF is real. The *Gaia* DR2 proper motion of 1457–086 is used together with the 2010 and 2013 NACO images to calculate the separation of background source over time, where it should be 0.1 arcsec in the 2006 IRAC image, and 0.7 arcsec in 2017. This is consistent with the roundness values over time.

The chance that the observed 30 μJy excess at 4.5 μm is caused by a background galaxy within 2.4 arcsec^2 of the target is one out of 760, following the method outlined in Farihi et al. (2008). Thus the probability that at least one star in the (195-star) sample has a background contamination similar to the excess seen at 1457–086 is 23 per cent. It should be noted that even in the case that 1457–086 has no detectable infrared excess beyond that of the background source, it is clear from the ongoing metal pollution that circumstellar material is present. This highlights the overall finding of this study, that discs are likely tenuous and subtle, while metal pollution is a much more sensitive tracer of circumstellar material.

5 CONCLUSIONS

A large and unbiased sample of white dwarfs was observed to determine the frequency of infrared excesses and atmospheric metals using *Spitzer* and *Hubble*, respectively. This study focused on the infrared data, where photometric measurements were evaluated using two methods, flux excess and colour excess. The flux excess proved more sensitive and seven sources were identified in this manner, while the colour excess method only discovered three candidates. Two stars with previously discovered infrared excesses (1457–086 and 2328+107) have a flux excess, but not a colour excess, and it is possible the photometric excesses arise from non-disc sources (i.e. companions). A further two stars without a colour excess are candidate binaries, as this is consistent with a steep slope at IRAC wavelengths. If correct, then only 0843+516, 1015+161, and 1018+410 remain as bona fide disc detections in the sample. Interestingly, these three stars are the only sources with greater than 3σ excesses via both methods. Future facilities that are sensitive to fainter infrared disc emission might benefit from a combination of these methods to distinguish genuine circumstellar discs from companions or background sources.

The frequency of infrared excesses due to debris discs over the single white dwarf sample is $1.5^{+1.5}_{-0.5}$ per cent, and broadly agrees with previous surveys, but on the lower end of prior estimates. The unbiased nature, size, and sensitivity of the study should make the result fairly definitive and robust relative to prior work. Another key result is that, in stark contrast to the modest infrared excess frequency, 45 ± 4 per cent of single stars in the *Hubble* COS subsample have atmospheric metals. This confirms prior studies indi-

cating that there is a large population of debris discs orbiting white dwarfs, but only a small fraction of these – roughly one out of 30 – are detectable in the infrared. The detection of atmospheric metals should be considered equivalent to the detection of (prior or current) circumstellar material.

For the white dwarfs in wide binaries, the infrared excess frequency is consistent with zero, but with an upper limit of 8 per cent. Atmospheric metals occur in 67^{+10}_{-15} per cent of similar sources, consistent with that measure for single stars in this study. Notably, the fraction of the local white dwarf population that is both polluted and in a binary is perfectly consistent with the fraction of field white dwarfs in binaries. Lastly and remarkably, the known dusty white dwarfs lack co-moving companions and thus their wide binary fraction (0 out of 40; binomial probability upper limit of 2.8 per cent) is strongly incompatible with that of the field. Thus, it does not appear that binarity is connected – even weakly – with atmospheric pollution in white dwarf stars. On the basis of this study and these facts, the delivery of planetary debris into the immediate vicinity of white dwarf stars and the subsequent surface pollution is likely controlled by major planets.

ACKNOWLEDGEMENTS

The authors would like to thank the anonymous referee for helpful comments that improved the manuscript. This work is based on observations made with the *Spitzer Space Telescope*, which is operated by the Jet Propulsion Laboratory, California Institute of Technology under a contract with NASA. Based on observations made with the NASA/ESA *Hubble Space Telescope*, obtained at the Space Telescope Science Institute, which is operated by the Association of Universities for Research in Astronomy, Inc., under NASA contract NAS 5-26555. These observations are associated with programs #12169, #12474, #13652, and #14077. T. G. Wilson and A. Swan acknowledge funding from STFC studentships. B. T. Gänsicke received financial support from the European Union's European Research Council, grant number 320964 (WDTracer).

REFERENCES

Ahn C. P., et al., 2012, ApJS, 203, 21
Barber S. D., Patterson A. J., Kilic M., Leggett S. K., Dufour P., Bloom J. S., Starr D. L., 2012, ApJ, 760, 26
Bédard A., Bergeron P., Fontaine G., 2017, ApJ, 848, 11
Bergfors C., Farihi J., Dufour P., Rocchetto M., 2014, MNRAS, 444, 2147
Bergin E. A., Blake G. A., Ciesla F., Hirschmann M. M., Li J., 2015, Proceedings of the National Academy of Science, 112, 8965
Bochkarev K. V., Rafikov R. R., 2011, ApJ, 741, 36
Bonsor A., Veras D., 2015, MNRAS, 454, 53
Bonsor A., Wyatt M. C., 2012, MNRAS, 420, 2990
Bonsor A., Farihi J., Wyatt M. C., van Lieshout R., 2017, MNRAS, 468, 154
Cauley P. W., Farihi J., Redfield S., Bachman S., Parsons S. G., Gänsicke B. T., 2018, ApJ, 852, L22
Chambers K. C., et al., 2016, preprint, (arXiv:1612.05560)
Cheselka M., Holberg J. B., Watkins R., Collins J., Tweedy R. W., 1993, AJ, 106, 2365
Cutri R. M., et al., 2003, VizieR Online Data Catalog, 2246
Debes J. H., 2006, ApJ, 652, 636
Debes J. H., Hoard D. W., Wachter S., Leisawitz D. T., Cohen M., 2011, ApJS, 197, 38
Debes J. H., Walsh K. J., Stark C., 2012, ApJ, 747, 148
Debes J. H., et al., 2019, ApJ, 872, L25
Dennihy E., Clemens J. C., Debes J. H., Dunlap B. H., Kilkenny D., O'Brien P. C., Fuchs J. T., 2017, ApJ, 849, 77
Drake A. J., et al., 2009, ApJ, 696, 870
Eggen O. J., Greenstein J. L., 1965a, ApJ, 141, 83
Eggen O. J., Greenstein J. L., 1965b, ApJ, 142, 925
El-Badry K., Rix H.-W., 2018, MNRAS, 480, 4884
Epchtein N., et al., 1999, A&A, 349, 236
Farihi J., 2009, MNRAS, 398, 2091
Farihi J., 2016, New Astron. Rev., 71, 9
Farihi J., Becklin E. E., Zuckerman B., 2005, ApJS, 161, 394
Farihi J., Zuckerman B., Becklin E. E., 2008, ApJ, 674, 431
Farihi J., Jura M., Zuckerman B., 2009, ApJ, 694, 805
Farihi J., Jura M., Lee J.-E., Zuckerman B., 2010, ApJ, 714, 1386
Farihi J., Gänsicke B. T., Koester D., 2013a, Science, 342, 218
Farihi J., Bond H. E., Dufour P., Haghighipour N., Schaefer G. H., Holberg J. B., Barstow M. A., Burleigh M. R., 2013b, MNRAS, 430, 652
Farihi J., Parsons S. G., Gänsicke B. T., 2017, Nature Astronomy, 1, 0032
Fazio G. G., et al., 2004, ApJS, 154, 10
Ferguson D. H., Green R. F., Liebert J., 1984, ApJ, 287, 320
Fontaine G., Brassard P., Bergeron P., 2001, PASP, 113, 409
Frewen S. F. N., Hansen B. M. S., 2014, MNRAS, 439, 2442
Gänsicke B. T., Koester D., Farihi J., Girven J., Parsons S. G., Breedt E., 2012, MNRAS, 424, 333
Gentile Fusillo N. P., et al., 2019, MNRAS, 482, 4570
Gianninas A., Bergeron P., Ruiz M. T., 2011, ApJ, 743, 138
Gillon M., et al., 2017, Nature, 542, 456
Girven J., Gänsicke B. T., Steeghs D., Koester D., 2011, MNRAS, 417, 1210
Greenstein J. L., 1974, AJ, 79, 964
Greenstein J. L., 1976, AJ, 81, 323
Greenstein J. L., 1984, ApJ, 276, 602
Hamers A. S., Portegies Zwart S. F., 2016, MNRAS, 462, L84
Harris H. C., et al., 2013, ApJ, 779, 21
Henden A. A., Templeton M., Terrell D., Smith T. C., Levine S., Welch D., 2016, VizieR Online Data Catalog, 2336
Hoard D. W., Wachter S., Sturch L. K., Widhalm A. M., Weiler K. P., Pretorius M. L., Wellhouse J. W., Gibiansky M., 2007, AJ, 134, 26
Hollands M. A., Gänsicke B. T., Koester D., 2018a, MNRAS, 477, 93
Hollands M. A., Tremblay P.-E., Gänsicke B. T., Gentile-Fusillo N. P., Toonen S., 2018b, MNRAS, 480, 3942
Jordan S., et al., 1998, A&A, 330, 277
Jura M., Young E. D., 2014, Annual Review of Earth and Planetary Sciences, 42, 45
Jura M., Farihi J., Zuckerman B., 2007, ApJ, 663, 1285
Jura M., Farihi J., Zuckerman B., 2009, AJ, 137, 3191
Jura M., Dufour P., Xu S., Zuckerman B., Klein B., Young E. D., Melis C., 2015, ApJ, 799, 109
Karl C., Napiwotzki R., Heber U., Lisker T., Nelemans G., Christlieb N., Reimers D., 2003, Double Degenerates from the Supernova IA Progenitor Survey (SPY). Springer Netherlands, Dordrecht, pp 43–46, doi:10.1007/978-94-010-0215-8_12
Kawka A., Vennes S., 2016, MNRAS, 458, 325
Kennedy G. M., Wyatt M. C., 2012, MNRAS, 426, 91
Kenyon S. J., Bromley B. C., 2017, ApJ, 839, 38
Kidder K. M., Holberg J. B., Mason P. A., 1991, AJ, 101, 579
Koester D., 2009, A&A, 498, 517
Koester D., 2010, Mem. Soc. Astron. Italiana, 81, 921
Koester D., Rollenhagen K., Napiwotzki R., Voss B., Christlieb N., Homeier D., Reimers D., 2005, A&A, 432, 1025
Koester D., Voss B., Napiwotzki R., Christlieb N., Homeier D., Lisker T., Reimers D., Heber U., 2009, A&A, 505, 441
Koester D., Gänsicke B. T., Farihi J., 2014, A&A, 566, A34
Lawrence A., et al., 2007, MNRAS, 379, 1599
Liebert J., Bergeron P., Holberg J. B., 2005, ApJS, 156, 47
Maoz D., Hallakoun N., 2017, MNRAS, 467, 1414
Marty B., et al., 2017, Science, 356, 1069
Maxted P. F. L., Marsh T. R., Moran C. K. J., 2000, MNRAS, 319, 305
Metzger B. D., Rafikov R. R., Bochkarev K. V., 2012, MNRAS, 423, 505

Mighell K. J., Glaccum W., Hoffmann W., 2008, in Space Telescopes and Instrumentation 2008: Optical, Infrared, and Millimeter. p. 70102W, doi:10.1117/12.789801
Mueller B. E. A., Bues I., 1987, Mitteilungen der Astronomischen Gesellschaft Hamburg, 70, 345
Mullally F., Kilic M., Reach W. T., Kuchner M. J., von Hippel T., Burrows A., Winget D. E., 2007, ApJS, 171, 206
Mustill A. J., Veras D., Villaver E., 2014, MNRAS, 437, 1404
Napiwotzki R., et al., 2003, The Messenger, 112, 25
Patel R. I., Metchev S. A., Heinze A., 2014, ApJS, 212, 10
Patel R. I., Metchev S. A., Heinze A., Trollo J., 2017, AJ, 153, 54
Petrovich C., Muñoz D. J., 2017, ApJ, 834, 116
Raddi R., Gänsicke B. T., Koester D., Farihi J., Hermes J. J., Scaringi S., Breedt E., Girven J., 2015, MNRAS, 450, 2083
Rafikov R. R., 2011a, MNRAS, 416, L55
Rafikov R. R., 2011b, ApJ, 732, L3
Reach W. T., Kuchner M. J., von Hippel T., Burrows A., Mullally F., Kilic M., Winget D. E., 2005, ApJ, 635, L161
Redfield S., Farihi J., Cauley P. W., Parsons S. G., Gänsicke B. T., Duvvuri G. M., 2017, ApJ, 839, 42
Rocchetto M., Farihi J., Gänsicke B. T., Bergfors C., 2015, MNRAS, 449, 574
Schultz G., Zuckerman B., Becklin E. E., 1996, ApJ, 460, 402
Smallwood J. L., Martin R. G., Livio M., Lubow S. H., 2018, MNRAS, 480, 57
Stephan A. P., Naoz S., Zuckerman B., 2017, ApJ, 844, L16
Subasavage J. P., Henry T. J., Jao W.-C., Nelan E. P., Harris H. C., Dahn C. C., 2009, in Journal of Physics Conference Series. p. 012017, doi:10.1088/1742-6596/172/1/012017
Tappert C., Gänsicke B. T., Schmidtobreick L., Ribeiro T., 2011, A&A, 532, A129
Vanderburg A., et al., 2015, Nature, 526, 546
Veras D., Mustill A. J., Bonsor A., Wyatt M. C., 2013, MNRAS, 431, 1686
Veras D., Leinhardt Z. M., Eggl S., Gänsicke B. T., 2015, MNRAS, 451, 3453
Veras D., Xu S., Rebassa-Mansergas A., 2018, MNRAS, 473, 2871
Wachter S., Hoard D. W., Hansen K. H., Wilcox R. E., Taylor H. M., Finkelstein S. L., 2003, ApJ, 586, 1356
Werner M. W., et al., 2004, ApJS, 154, 1
Wilson D. J., Gänsicke B. T., Farihi J., Koester D., 2016, MNRAS, 459, 3282
Xu S., Jura M., 2012, ApJ, 745, 88
Xu S., Zuckerman B., Dufour P., Young E. D., Klein B., Jura M., 2017, ApJ, 836, L7
Zuckerman B., 2014, ApJ, 791, L27
Zuckerman B., Becklin E. E., 1992, ApJ, 386, 260
Zuckerman B., Koester D., Reid I. N., Hünsch M., 2003, ApJ, 596, 477
Zuckerman B., Melis C., Klein B., Koester D., Jura M., 2010, ApJ, 722, 725

APPENDIX A: SUPPLEMENTARY MATERIAL

Table A1: *Spitzer* IRAC fluxes for white dwarfs in this sample, together with an indication of atmospheric Si II observed by *Hubble* COS. Stellar parameters and binary type are taken from the literature.

WD	$T_{\rm eff}$ (K)	m mag)	log $[t_{\rm cool}$ (yr)]	$F_{3.6\,\mu m}$ (μJy)	$F_{4.5\,\mu m}$ (μJy)	$F_{5.7\,\mu m}$ (μJy)	$F_{7.9\,\mu m}$ (μJy)	Si II	Binarity
0000+171	20 200	15.8	7.76	64 ± 3	44 ± 2	–	–	Y	–
0002+165	25 900	15.7	7.28	65 ± 3	40 ± 2	–	–	Y	–
0004+061	24 400	16.1	7.91	55 ± 3	33 ± 2	–	–	N	–
0013–241	18 500	15.4	8.00	103 ± 5	66 ± 4	–	–	N	–
0017+061[b]	28 100	15.2	7.08	2400 ± 100	1620 ± 80	–	–	–	MS, 1
0018–339	20 600	14.6	7.69	200 ± 10	120 ± 6	–	–	N	–
0028–474[c]	17 400	15.2	7.87	166 ± 8	104 ± 5	–	–	N	WD, 2
0047–524	18 800	14.2	7.83	–	190 ± 10	–	66 ± 3	N	–
0048–544	17 900	15.2	7.87	125 ± 6	81 ± 4	–	–	–	–
0048+202	20 400	15.4	7.83	102 ± 5	65 ± 3	–	–	–	–
0052–147	26 700	15.1	7.68	106 ± 5	68 ± 3	–	–	N	–
0059+257	21 400	15.9	7.77	68 ± 4	44 ± 2	–	–	Y	–
0102+095	24 800	14.4	7.45	220 ± 10	147 ± 7	–	–	Y	–
0106–358[a]	30 900	14.7	7.04	159 ± 8	91 ± 5	–	–	Y	MS, 3
0110–139	26 300	15.8	7.38	60 ± 3	40 ± 2	–	–	–	–
0114–605[c]	24 700	15.1	7.30	113 ± 6	75 ± 4	–	–	Y	WD, 4
0124–257	23 000	16.2	7.43	36 ± 2	26 ± 1	–	–	N	–
0127–050	16 800	14.9	8.16	177 ± 9	112 ± 6	–	–	–	–
0127+270	24 900	15.9	7.36	55 ± 3	33 ± 2	25	38	–	–
0129–205	20 000	15.3	7.79	104 ± 5	68 ± 4	–	–	–	–
0131+018[c]	15 200	14.5	8.40	340 ± 20	220 ± 10	–	–	N	WD, 2
0136+768	16 900	14.8	7.95	230 ± 10	151 ± 8	–	–	N	–
0140–392	21 800	14.4	7.62	250 ± 10	165 ± 8	–	–	Y	–
0145–257[b]	26 700	14.5	7.20	8100 ± 400	5400 ± 300	–	–	–	MS, 5
0155+069	22 000	15.5	7.41	108 ± 6	68 ± 3	–	–	N	–
0200+248	23 300	15.7	7.79	110 ± 10	71 ± 8	–	–	N	–
0201–052	24 600	16.0	7.32	41 ± 2	28 ± 2	–	–	–	–
0216+143	26 900	14.6	7.26	210 ± 10	130 ± 7	80 ± 10	33	N	–
0221–055[b]	25 800	16.2	7.52	62 ± 3	42 ± 2	–	–	–	WD, 4
0222–265	23 200	15.7	7.60	76 ± 4	51 ± 3	–	–	–	–
0227+050	19 300	12.8	7.83	–	780 ± 40	–	260 ± 10	–	–
0229+270	24 200	15.5	7.36	80 ± 4	51 ± 3	–	–	–	–
0231–054	17 300	14.3	8.86	–	240 ± 10	–	71 ± 4	N	–
0242–174	20 700	15.4	7.79	96 ± 5	62 ± 3	–	–	Y	–
0300–232	22 400	15.7	8.03	72 ± 4	44 ± 2	–	–	–	–
0305–117	26 800	16.0	7.18	53 ± 3	33 ± 2	–	–	N	–
0307+149[a]	21 400	15.4	7.61	112 ± 6	71 ± 4	–	–	Y	WD, 6
0308–230	23 600	15.1	8.14	108 ± 5	70 ± 4	–	–	N	–
0308+188	18 500	14.2	7.89	320 ± 20	200 ± 10	–	–	N	–
0316+345	15 400	14.2	7.98	–	230 ± 10	–	74 ± 9	N	–
0331+226	21 500	15.3	7.43	110 ± 6	71 ± 4	–	–	–	–
0341+021[c]	22 200	15.4	7.27	102 ± 5	61 ± 3	–	–	Y	WD, 7
0345+134	25 100	16.1	7.56	46 ± 2	29 ± 2	–	–	–	–
0349–256	21 000	15.7	7.73	72 ± 4	47 ± 2	–	–	–	–
0352+018	22 100	15.6	7.28	79 ± 4	50 ± 3	–	–	Y	–
0358–514	23 400	15.7	7.46	70 ± 4	47 ± 2	–	–	N	–
0400+148	14 600	14.9	8.54	200 ± 10	130 ± 7	–	–	N	–
0403–414	22 700	16.4	7.54	41 ± 2	26 ± 1	–	–	Y	–
0406+169	15 800	15.3	8.46	126 ± 6	78 ± 4	53 ± 5	44 ± 6	N	–
0410+117[a]	21 100	13.9	7.58	–	250 ± 10	–	64 ± 3	Y	MS, 6
0414–406	20 900	16.1	7.79	48 ± 3	30 ± 2	–	–	N	–
0416–105	24 900	15.4	7.26	87 ± 4	53 ± 3	–	–	Y	–
0418–534	27 100	16.4	7.15	32 ± 2	21 ± 1	–	–	Y	–
0418–103	23 400	15.7	7.94	70 ± 4	44 ± 2	–	–	N	–
0421+162	19 600	14.3	7.93	280 ± 10	172 ± 9	115 ± 6	60 ± 5	Y	–

Table A1 – continued from previous page

WD	$T_{\rm eff}$ (K)	m (mag)	log [$t_{\rm cool}$ (yr)]	$F_{3.6\,\mu m}$ (μJy)	$F_{4.5\,\mu m}$ (μJy)	$F_{5.7\,\mu m}$ (μJy)	$F_{7.9\,\mu m}$ (μJy)	Si II	Binarity
0431+126	21 400	14.2	7.75	–	177 ± 9	–	34 ± 7	Y	–
0452–347	21 200	16.1	7.62	57 ± 3	37 ± 2	–	–	Y	–
0455–532	24 400	16.8	7.22	31 ± 2	18 ± 1	–	–	–	–
0507+045A[a]	20 800	14.2	7.82	–	210 ± 10	–	140 ± 10	Y	WD, 8
0730+487	14 900	14.8	8.78	210 ± 10	129 ± 7	86 ± 6	56	N	–
0732–427	15 600	14.2	8.39	–	250 ± 10	–	90 ± 20	N	–
0816+297	16 700	15.8	8.06	78 ± 4	52 ± 3	26	26	N	–
0817+386	25 200	15.8	7.30	65 ± 4	42 ± 2	–	–	N	–
0821+632	16 800	15.9	8.01	72 ± 4	46 ± 2	–	–	N	–
0839+231	25 800	14.5	7.20	210 ± 10	131 ± 7	–	–	Y	–
0843+516	23 900	16.0	7.56	136 ± 7	137 ± 7	102 ± 7	159 ± 9	Y	–
0846+557	27 400	16.4	7.11	33 ± 2	18 ± 1	–	–	N	–
0854+404	22 300	14.8	7.58	156 ± 8	97 ± 5	–	–	Y	–
0859–039	23 700	13.2	7.38	700 ± 40	440 ± 20	–	–	–	–
0859+337	25 400	16.6	7.49	32 ± 2	19 ± 1	–	–	–	–
0904+391	26 200	16.3	7.40	33 ± 3	23 ± 2	–	–	N	–
0915+526	15 600	15.5	8.27	107 ± 5	65 ± 3	–	–	N	–
0920+363	24 100	16.1	7.22	56 ± 3	35 ± 2	–	–	Y	–
0922+183	24 700	16.4	7.48	40 ± 2	24 ± 2	–	–	–	–
0933+025[b]	22 400	15.9	7.78	3600 ± 200	2500 ± 100	–	–	N	MS, 10
0938+550	18 500	14.8	8.04	200 ± 10	123 ± 6	–	–	–	–
0944+192	17 400	14.5	8.16	250 ± 10	159 ± 8	–	–	N	–
0947+325	22 100	15.5	8.04	87 ± 4	57 ± 3	–	–	N	–
0954+697	21 400	16.0	7.60	63 ± 3	44 ± 2	–	–	Y	–
0956+020	15 700	15.7	8.13	88 ± 5	54 ± 3	–	–	N	–
1003–023	20 600	15.3	7.83	121 ± 6	73 ± 4	–	–	–	–
1005+642	19 700	13.7	7.88	460 ± 20	290 ± 10	–	–	N	–
1012–008	23 200	15.6	7.72	80 ± 4	49 ± 3	–	–	–	–
1013+256	22 000	16.3	7.68	42 ± 2	23 ± 1	–	–	Y	–
1015+161	20 000	15.6	7.99	200 ± 10	167 ± 8	142 ± 8	124 ± 7	Y	–
1016–308	16 300	14.6	8.37	240 ± 10	153 ± 8	–	–	–	–
1017+125[a]	21 400	15.7	7.73	73 ± 4	49 ± 3	28 ± 3	19 ± 6	Y	WD, 3
1018+410	23 700	16.4	7.82	86 ± 4	76 ± 4	–	–	–	–
1020–207	19 900	15.0	7.78	130 ± 7	84 ± 4	–	–	Y	–
1034+492	20 700	15.4	7.97	101 ± 5	59 ± 3	49 ± 4	30	Y	–
1038+633	24 500	15.2	8.00	109 ± 5	67 ± 3	57 ± 4	27	Y	–
1049–158	20 600	14.4	8.24	260 ± 10	155 ± 8	–	–	N	–
1049+103[c]	20 600	15.8	7.71	3700 ± 200	2600 ± 100	–	–	N	MS, 1
1052+273	23 100	14.1	8.04	300 ± 10	190 ± 10	130 ± 7	59 ± 7	N	–
1058–129	24 300	14.9	8.20	128 ± 7	82 ± 4	42 ± 6	30 ± 8	N	–
1102+748	19 700	15.1	8.24	136 ± 7	90 ± 5	–	–	N	–
1104+602	17 900	13.7	8.11	460 ± 20	290 ± 10	–	–	N	–
1105–048[a]	15 100	13.1	8.18	–	640 ± 30	–	260 ± 20	–	MS, 11
1113+413	25 400	15.4	7.30	96 ± 5	61 ± 3	–	–	Y	–
1115+166	22 100	15.1	7.72	134 ± 7	86 ± 4	65 ± 6	44	N	–
1117–023	14 700	14.5	8.31	290 ± 10	180 ± 9	–	–	N	–
1120+439	27 000	15.4	7.63	84 ± 4	48 ± 3	55	50	–	–
1122–324	21 700	15.8	7.58	62 ± 3	40 ± 2	–	–	–	–
1126+384	25 200	14.9	7.34	127 ± 6	76 ± 4	–	–	Y	–
1128+564	26 600	16.5	7.18	30 ± 2	19 ± 1	–	–	N	–
1129+155	17 700	14.1	7.98	380 ± 20	230 ± 10	159 ± 9	78 ± 7	Y	–
1132+470	27 500	16.4	8.28	66 ± 3	42 ± 2	–	–	–	–
1133+293	23 000	14.9	7.52	147 ± 7	91 ± 8	64 ± 7	44 ± 8	Y	–
1134+300	21 300	12.5	8.22	1380 ± 70	890 ± 40	–	–	–	–
1136+139	23 900	16.8	7.43	23 ± 3	16 ± 2	–	–	–	–
1143+321[a]	15 900	13.7	8.25	740 ± 40	480 ± 30	–	–	N	MS, 12
1145+187	26 600	14.2	7.18	240 ± 10	143 ± 7	–	–	Y	–
1152+371	27 400	14.7	8.47	13 ± 2	10 ± 1	–	–	–	–

Table A1 – continued from previous page

WD	$T_{\rm eff}$ (K)	m (mag)	log [$t_{\rm cool}$ (yr)]	$F_{3.6\,\mu m}$ (μJy)	$F_{4.5\,\mu m}$ (μJy)	$F_{5.7\,\mu m}$ (μJy)	$F_{7.9\,\mu m}$ (μJy)	Si II	Binarity
1201–001	19 800	15.2	8.17	124 ± 6	80 ± 4	48 ± 3	18 ± 4	–	–
1202+308	28 900	16.3	7.04	40 ± 2	26 ± 2	–	–	N	–
1204–322	21 300	15.6	7.79	80 ± 4	52 ± 3	–	–	–	–
1220+234	26 500	15.6	7.74	67 ± 3	43 ± 2	–	–	N	–
1224+309[c]	28 800	16.2	7.08	610 ± 30	410 ± 20	–	–	Y	MS, 13
1229–012	19 400	14.5	7.60	240 ± 10	153 ± 8	91 ± 6	64 ± 8	N	–
1230–308	22 800	15.7	7.41	70 ± 4	46 ± 2	–	–	N	–
1232+479	14 400	14.5	8.31	280 ± 10	173 ± 9	–	–	–	–
1233–164[c]	24 900	15.1	7.66	114 ± 6	73 ± 4	–	–	N	WD, 4
1241+235	26 700	15.7	7.20	76 ± 4	53 ± 3	–	–	–	–
1243+015	21 600	16.5	7.72	34 ± 2	23 ± 1	–	–	Y	–
1247–115	28 100	15.3	7.23	88 ± 4	54 ± 3	–	–	Y	–
1249+160	25 600	14.7	7.24	177 ± 9	107 ± 5	–	–	Y	–
1249+182	19 900	15.2	7.74	95 ± 5	60 ± 3	–	–	Y	–
1257+047[a]	21 800	14.9	7.61	151 ± 8	98 ± 5	–	–	Y	MS, 3
1305+018[b]	29 000	15.2	7.26	110 ± 6	77 ± 4	–	–	–	MS, 14
1308–301	15 300	15.2	8.34	155 ± 8	96 ± 5	–	–	Y	–
1310–305	20 400	14.5	7.83	220 ± 10	143 ± 7	–	–	Y	–
1314–153	15 700	14.9	8.16	210 ± 10	134 ± 7	–	–	N	–
1323–514	19 400	14.4	7.80	280 ± 10	176 ± 9	–	–	Y	–
1325–089	17 000	15.0	8.01	165 ± 8	107 ± 5	–	–	Y	–
1325+279	21 300	15.8	7.91	64 ± 7	42 ± 5	–	–	Y	–
1330+473	22 500	15.2	7.57	106 ± 6	70 ± 4	–	–	N	–
1333+497	29 300	15.7	7.08	58 ± 3	36 ± 2	–	–	–	–
1334–160[a]	18 700	15.4	8.27	116 ± 7	94 ± 6	–	–	–	MS, 6
1334+070[c]	16 900	15.4	7.63	162 ± 8	99 ± 5	–	–	N	WD, 2
1335+369	20 500	14.8	7.62	210 ± 10	135 ± 7	–	–	–	–
1337+705	20 500	12.6	7.76	–	710 ± 40	–	250 ± 10	–	–
1338+081	24 400	16.4	7.34	31 ± 2	19 ± 1	–	–	–	–
1339+346[d]	16 000	15.9	8.08	1030	–	–	–	N	–
1349+144[c]	16 600	15.3	8.16	134 ± 7	84 ± 4	–	–	N	WD, 15
1353+409	23 500	15.5	7.38	77 ± 4	50 ± 3	33 ± 5	26 ± 5	N	–
1408+323	18 200	14.0	7.97	–	250 ± 10	–	92 ± 7	Y	–
1412–109[b]	25 700	15.9	7.38	760 ± 40	530 ± 30	330 ± 20	220 ± 20	Y	MS, 16
1421+318	27 200	15.4	7.23	82 ± 4	52 ± 3	–	–	Y	–
1433+538[c]	22 400	16.1	7.43	900 ± 50	600 ± 30	–	–	–	MS, 17
1449+168	22 400	15.4	7.58	91 ± 5	58 ± 3	–	–	–	–
1451+006	25 500	15.3	7.30	99 ± 5	63 ± 3	–	–	Y	–
1452–042	23 500	16.3	7.83	51 ± 3	36 ± 2	–	–	–	–
1452+553	28 300	16.1	7.60	43 ± 2	28 ± 2	–	–	Y	–
1457–086	20 400	15.8	7.72	114 ± 6	74 ± 4	49 ± 6	53	Y	–
1459+347	21 500	15.8	8.20	66 ± 3	41 ± 2	–	–	N	–
1507+220	19 900	15.0	7.80	151 ± 8	97 ± 5	–	–	–	–
1508+548	17 000	15.7	8.13	80 ± 4	50 ± 3	–	–	N	–
1511+009	27 600	15.9	7.26	56 ± 3	34 ± 2	–	–	–	–
1513+442	29 200	15.2	7.15	82 ± 4	52 ± 3	–	–	Y	–
1517+373	25 400	16.3	7.38	41 ± 2	29 ± 2	–	–	–	–
1518–003	15 400	15.2	8.16	122 ± 6	78 ± 4	–	–	N	–
1524–749	23 100	16.0	7.36	64 ± 3	39 ± 2	–	–	N	–
1525+257	22 300	15.7	7.97	70 ± 4	45 ± 2	–	–	N	–
1527+090	21 200	14.3	7.72	260 ± 10	165 ± 8	–	–	Y	–
1531–022	18 600	14.0	7.92	–	240 ± 10	–	103 ± 8	N	–
1533–057	20 000	15.4	8.07	95 ± 5	58 ± 3	–	–	Y	–
1535+293	24 500	15.9	7.40	51 ± 3	30 ± 2	–	–	N	–
1539+530[b]	26 800	15.6	7.43	5200 ± 300	3400 ± 200	–	–	–	MS, 3
1547+057	24 400	15.9	8.00	57 ± 3	36 ± 2	–	–	N	–
1548+149	21 500	15.2	7.74	123 ± 6	77 ± 4	–	–	Y	–
1550+183	14 300	14.8	8.62	220 ± 10	136 ± 7	95 ± 7	53 ± 6	N	–

Table A1 – continued from previous page

WD	$T_{\rm eff}$ (K)	m (mag)	log $[t_{\rm cool}$ (yr)]	$F_{3.6\,\mu{\rm m}}$ (μJy)	$F_{4.5\,\mu{\rm m}}$ (μJy)	$F_{5.7\,\mu{\rm m}}$ (μJy)	$F_{7.9\,\mu{\rm m}}$ (μJy)	Si II	Binarity
1553+353	25 600	14.8	7.30	169 ± 8	105 ± 5	62 ± 5	43	–	–
1554+215[a]	26 300	15.2	7.26	105 ± 6	63 ± 4	–	–	–	MS, 6
1555–089[a]	14 600	14.8	8.30	220 ± 13	134 ± 8	–	–	N	MS, 18
1601+581	14 700	13.8	8.27	520 ± 30	330 ± 10	–	–	Y	–
1609+044	29 100	15.2	7.08	96 ± 5	59 ± 3	–	–	N	–
1614–128	16 600	15.0	8.01	161 ± 8	104 ± 5	–	–	N	–
1614+136	22 000	15.2	7.23	113 ± 6	68 ± 4	54 ± 5	16 ± 6	–	–
1619+123[a]	16 400	14.6	8.03	230 ± 10	149 ± 8	–	–	N	MS, 3
1620–391[a]	24 700	11.0	7.38	5000 ± 200	3100 ± 200	1900 ± 100	1070 ± 50	–	MS, 6
1620+260	28 300	15.6	7.15	76 ± 4	46 ± 2	–	–	N	–
1633+676	23 700	16.3	7.53	34 ± 2	22 ± 1	–	–	N	–
1641+387	15 600	14.6	8.31	250 ± 10	156 ± 8	–	–	Y	–
1643+143[c]	26 800	15.4	7.26	5700 ± 300	3800 ± 200	–	–	–	MS, 19
1647+375	22 000	14.9	7.59	138 ± 7	86 ± 4	–	–	Y	–
1713+332	22 100	14.4	7.32	–	185 ± 9	–	57 ± 6	Y	–
1713+695	15 900	13.2	8.26	820 ± 40	520 ± 30	–	–	N	–
1739+804	26 500	15.6	7.45	82 ± 4	50 ± 3	–	–	N	–
1755+194	24 400	16.0	7.46	55 ± 3	34 ± 2	–	–	Y	–
1914–598	19 800	14.4	7.88	290 ± 10	200 ± 10	–	–	Y	–
1919+145	15 300	13.0	8.40	1120 ± 60	690 ± 30	1180	741	N	–
1943+163	19 800	14.0	7.71	–	230 ± 10	–	101 ± 8	Y	–
1953–715	19 300	15.1	7.96	133 ± 7	84 ± 4	–	–	Y	–
2009+622[c]	26 500	15.3	7.15	1330 ± 70	900 ± 50	–	–	Y	MS, 20
2018–233	15 700	15.1	8.27	170 ± 9	111 ± 6	–	–	N	–
2021–128	20 800	15.2	7.78	113 ± 6	74 ± 4	–	–	N	–
2032+188	18 200	15.3	7.58	125 ± 6	81 ± 4	–	–	N	–
2039–682	17 100	13.3	8.51	–	490 ± 30	–	160 ± 10	N	–
2039–202	19 700	12.3	7.82	–	1040 ± 50	–	370 ± 20	–	–
2043–635	27 700	15.6	7.89	72 ± 4	49 ± 3	–	–	N	–
2046–220	23 400	15.4	7.45	89 ± 5	56 ± 3	–	–	Y	–
2056+073	27 300	15.4	7.75	80 ± 4	53 ± 3	–	–	N	–
2058+181	17 400	15.2	8.07	149 ± 8	97 ± 5	–	–	Y	–
2115+010	25 200	15.6	7.30	70 ± 4	43 ± 2	–	–	–	–
2134+218	18 000	14.5	8.06	–	159 ± 8	–	61 ± 7	Y	–
2143+353	26 100	15.9	7.38	51 ± 3	35 ± 2	–	–	N	–
2149+021	17 900	12.8	8.07	–	780 ± 40	–	270 ± 10	–	–
2152–045	19 800	15.7	7.44	84 ± 4	53 ± 3	–	–	Y	–
2200–136[c]	25 800	15.3	7.19	107 ± 5	65 ± 3	–	–	–	WD, 2
2204+070	25 600	15.8	7.49	70 ± 5	43 ± 2	–	–	–	–
2204+071	24 500	15.8	7.34	69 ± 4	42 ± 2	–	–	–	–
2205–139	26 000	15.0	7.69	120 ± 6	72 ± 4	–	–	N	–
2210+233	23 200	15.8	7.97	60 ± 3	35 ± 2	–	–	N	–
2218–271	15 000	14.7	8.14	350 ± 20	260 ± 10	–	–	N	–
2220+133	22 600	15.6	8.03	75 ± 4	46 ± 2	–	–	N	–
2220+217A[a]	18 700	15.5	8.29	80 ± 4	46 ± 2	–	–	–	WD, 2
2220+217B[a]	14 600	15.2	8.13	73 ± 4	43 ± 2	–	–	–	WD, 2
2225+219	26 000	15.8	7.30	60 ± 3	36 ± 2	–	–	Y	–
2226+061	15 300	14.8	7.93	200 ± 10	126 ± 6	73 ± 7	41	N	–
2229+235	19 300	16.0	8.03	59 ± 3	39 ± 2	24 ± 2	–	Y	–
2231–267	21 600	15.0	7.79	162 ± 8	109 ± 5	–	–	Y	–
2238–045	17 500	16.9	8.39	23 ± 1	13 ± 1	–	–	N	–
2244+210	24 100	16.5	7.41	35 ± 2	21 ± 1	–	–	Y	–
2248–504[c]	16 300	15.0	8.19	159 ± 8	100 ± 5	–	–	N	WD, 4
2257+162[c]	24 600	16.0	7.24	420 ± 20	290 ± 10	200 ± 10	128 ± 8	Y	MS, 9
2306+124	20 400	15.1	7.87	124 ± 6	77 ± 4	–	–	Y	–
2312–356	15 100	15.5	8.28	126 ± 6	83 ± 4	–	–	–	–
2318–226	29 900	16.1	7.15	40 ± 2	24 ± 1	–	–	–	–
2322–181	21 700	15.3	7.57	100 ± 5	62 ± 3	–	–	Y	–
2328+107	21 000	15.8	7.74	116 ± 6	77 ± 4	–	–	N	–

Table A1 – continued from previous page

WD	$T_{\rm eff}$ (K)	m (mag)	log $[t_{\rm cool}$ (yr)]	$F_{3.6\,\mu m}$ (μJy)	$F_{4.5\,\mu m}$ (μJy)	$F_{5.7\,\mu m}$ (μJy)	$F_{7.9\,\mu m}$ (μJy)	Si II	Binarity
2331+290	27 300	15.7	6.96	69 ± 4	43 ± 2	29	14	–	–
2345–481	29 400	15.5	6.86	54 ± 3	32 ± 2	–	–	N	–
2345+304	29 100	16.4	7.06	43 ± 2	27 ± 2	–	–	N	–
2347–192	27 400	16.1	7.23	41 ± 2	23 ± 1	–	–	–	–
2350–248	29 700	15.4	7.54	77 ± 4	50 ± 3	–	–	Y	–
2359–324[c]	22 500	16.3	7.38	43 ± 2	28 ± 2	–	–	N	WD, 4

Notes. Cooling ages are calculated using white dwarf evolutionary models (Fontaine, Brassard & Bergeron 2001) with stellar parameters derived from *Gaia* DR2 (Gentile Fusillo et al. 2019). Fluxes without reported errors are upper limits. Confirmed and candidate companions are labelled as MS (= main-sequence star, most of which are M dwarfs), and WD (= white dwarf).

[a] Common proper-motion binary resolved in IRAC images. Reliable photometry was recovered for the target via aperture photometry or APEX.

[b] Common proper-motion binary resolved in *Gaia* DR2. IRAC images fail to reveal both sources, and thus the point-source photometry reported may not be reliable.

[c] Confirmed or candidate short-period binary. *Gaia* DR2 does not resolve any additional components, and IRAC images are point-like.

[d] Photometry contaminated by background source.

References. (1) Zuckerman & Becklin (1992); (2) Koester et al. (2009); (3) Farihi et al. (2005); (4) Maoz & Hallakoun (2017); (5) Mueller & Bues (1987); (6) El-Badry & Rix (2018); (7) Maxted, Marsh & Moran (2000); (8) Jordan et al. (1998); (9) Wachter et al. (2003); (10) Schultz et al. (1996); (11) Greenstein (1984); (12) Eggen & Greenstein (1965a); (13) Ferguson, Green & Liebert (1984); (14) Cheselka et al. (1993); (15) Karl et al. (2003); (16) Hoard et al. (2007); (17) Greenstein (1976); (18) Eggen & Greenstein (1965b); (19) Kidder, Holberg & Mason (1991); (20) Greenstein (1974).

This paper has been typeset from a TEX/LATEX file prepared by the author.